



Investigation of electronic, optical, and thermoelectric properties of new d^0 half-metallic half-Heusler alloys SiLiX ($X = \text{Ca}$ and Sr)

Djelti Radouan¹ · Besbes Anissa² · Bestani Benaouda²

Received: 30 April 2021 / Accepted: 18 June 2021 / Published online: 16 August 2021
© Qatar University and Springer Nature Switzerland AG 2021

Abstract

The electronic, optical, and transport properties of new d^0 half-Heusler alloys SiLiX ($X = \text{Ca}, \text{Sr}$) were studied by using the first-principles method and semi-classical Boltzmann theory. The results of the electronic properties reveal for both half-Heusler the half-metallic ferromagnetic nature (HMF) with a direct gap of 1.401 eV and large half-metallic gap of 0.42 eV for SiLiSr alloy, while the SiLiCa compound shows an indirect band gap of 1.209 eV and half-metallic gap of 0.21 eV. The same magnetic moment of 1.00 μB per formula was observed for the two alloys. The optical computations indicate that SiLiX half-Heusler is active in a wide area of the electromagnetic spectrum. The high reflectivity of SiLiX alloys, which is well above 43% in the ultraviolet region and 38% in the near infrared region, let us use them as an effective shield in these domains. Around 300 K, the thermal conductivity was reduced by approximately 54%, following the replacement of calcium by strontium in the X site. The zT values very close to unity were reported in large temperature range. The obtained results reveal that the studied materials could be used efficiently for the applications of optical and thermoelectric devices.

Keywords Half-Heusler · d^0 half-metallic · Dielectric constant · Absorption coefficient · Merit factor

1 Introduction

De Groot et al. [1] established the notion of half-metallic ferromagnets for the first time, since then several researchers paid particular attention to the magnetic half-Heusler compounds due to their good thermoelectric [2–5] and optical properties [6–9]. Thereafter, the detection of d^0 (or sp) half-metallic ferromagnet (HM-FM) alloys, which imply only the “s” and “p” block elements, has challenged the understanding of magnetism and led the researchers to review the role of transition metals in controlling the magnetism, since, several theoretical studies based on density functional theory have been carried out [10–19]. Beldi et al. [20] have found magnetism in d^0 half-Heusler GeNaZ compounds ($Z = \text{Ca}, \text{Sr},$ and Ba) while the elements that compose these alloys are not magnetic. In their study of the impact of doping by silicon of d^0 half-Heusler KCaC , Hoat et al. [21] found that

the increase in Si rate decreases the half-metallic band gap value, which can minimize the stability of half-metallicity. Benabboun et al. [22] have explored the magnetic behavior of d^0 half-Heusler XCaZ ($X = \text{Li}, \text{Na}; Z = \text{B}, \text{C}$) and confirm that the magnetism comes from the spin polarization of atomic p orbitals, which persists in the alloys of calcium due to its large atomic radii. For the d^0 half-Heusler CNaCa , Wei et al. [23] confirm that its large half-metallic gap value of 0.609 eV guarantees it the stability of half-metallicity at room temperature. In the same context, the d^0 half-Heusler alloy LiCaC presents a large half-metallic gap of 0.53 eV and its half-metallicity can be retained for lattice compression up to 9.5% [24]. According to Vahabzadeh et al. [25], the low loss energy obtained in a wide range of wavelengths associated to a high absorption in these regions of the terminations [111] makes Zr_2TiSi films [111] suitable cases for optoelectronic applications. Ilkhani et al. [26] have investigated the transport properties of PdZrTiAl quaternary Heusler and confirm that the best thermoelectric performances estimated by the merit factor (which take in account the electronic and lattice thermal conductivity) are located around the room temperature. Rai et al. [27] investigated a series of Heusler compounds based cobalt and show that $\text{LSDA} + \text{U}$ and mBJ as compared to the conventional GGA widen the

✉ Djelti Radouan
djeltired@yahoo.fr; Radouane.djelti@univ-mosta.dz

¹ Technology and Solids Properties Laboratory, University of Mostaganem (UMAB) - Algeria, Mostaganem, Algeria

² SEA2M Laboratory, University of Mostaganem (UMAB) - Algeria, Mostaganem, Algeria

half-metallic gaps reasonably, while the magnetic moments within GGA and mBJ are almost same. The electron-core hole interaction has been found essential for describing the X-ray absorption and magnetic circular dichroism spectra at the L2, 3 edges of Cu and Mn in the $\text{Cu}_2\text{MnAl}_{1-x}\text{Ga}_x$ compound [28]. The role of DFT + U correction in Heusler alloys can be illustrated via the study conducted by Rai et al. [29–31] which show that the application of GGA + U under variable pressures on Fe_2CoAl compound radically changes the profile of the electronic structure which passes from a magnetic metal to a ferromagnetic half-metal with a total magnetic moment of $4.0 \mu\text{B}$. The main motivation of this study comes from this brief bibliographic review which shows that the optical and thermoelectric properties of the d^0 half-Heuslers have not been widely studied, comparatively to their magnetic properties and also to the half-Heuslers compounds with d- and f-orbital. The paper is drafted as follows: the computation details are given in Sect. 2, the results and discussion are presented in Sect. 3, and a brief summary of the results is given in Sect. 4.

2 Computational method

First-principles calculations founded on DFT have been conducted to determine the structural, electronic, optical, and thermoelectric properties of SiLiX ($X = \text{Ca}$ and Sr) half-Heusler. The exchange–correlation effects were treated with the general gradient approximation (GGA) using Perdew–Burke–Emzerhoff (PBE) functional [32]. The valence electrons for the SiLiX primal cell are $3s^2 3p^2$ of Si, $2s^1$ of Li, $4s^2$ of Ca, and $5s^2$ of Sr. The muffin tin radius (R_{MT}) values of 1.85, 2.1, and 2.5 Bohr were used for Si, Li, and X respectively. Other parameters such as $R_{\text{MT}} \times$ wave-vector, k-point mesh (K_{MAX}), and the maximum value of angular momentum (l_{max}) were selected to 7.0, $16 \times 16 \times 16$, and 10 respectively. The optical constants are derived from the complex dielectric function [23–35]. The semi-classical Boltzmann approach [36] as given in the BoltzTraP code was used to investigate the thermoelectric response of SiLiX compound. A fine grid mesh ($46 \times 46 \times 46$) was used.

3 Results and discussion

3.1 Structural properties

The ternary half-Heusler alloys SiLiX ($X = \text{Ca}$ and Sr) crystallize in the fcc structure with the space group $F\bar{4}3m(N^\circ.216)$. The optimization has been done in the paramagnetic (PM) and ferromagnetic (FM) configurations associated to the three possible types of atomic arrangement (α , β , and γ). From Fig. 1, which give the evolution

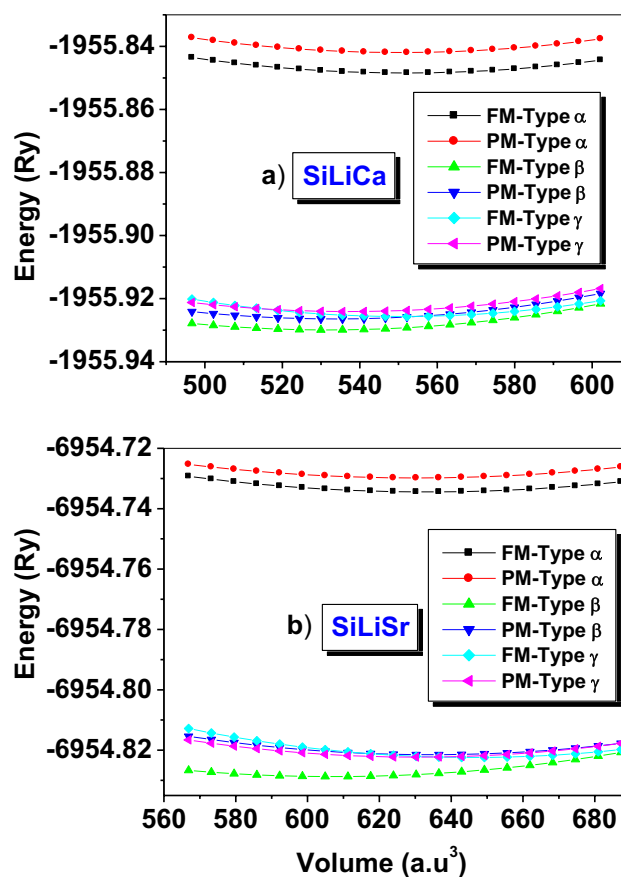


Fig. 1 Total energy as a function of volume for **a** SiLiCa and **b** SiLiSr half-Heusler alloy in the ferromagnetic (FM) and paramagnetic (PM) phases

of energy versus volume at zero pressure, we can see that the SiLiX ($X = \text{Ca}, \text{Sr}$) alloys are most stable in the β -type structure than in the α and γ -type structures. In addition, the ferromagnetic (FM) states are most energetically stable as it has the lower energies than the paramagnetic states (PM). In the following, we will calculate all properties only in ferromagnetic (FM) state β -type. The obtained structural parameters are listed in Table 1, where we can observe that the lattice parameter of SiLiSr is higher than that of SiLiCa , and the bulk modulus values of 30.28 GPa and 25.83 GPa obtained for SiLiCa and SiLiSr respectively suggest that these alloys are easily to compressible. These values are in the same magnitude order as those of other d^0 half-Heusler compounds; let us quote by way of example the LiNaN (43.7 GPa), LiKN (27.4 GPa) [37], N_2BaCs (39 GPa), N_2BaRb (38 GPa) [38], KCaC (34.72 GPa) [39], and LiMgBi (32.61 GPa) [40]. It should be specified that the negative enthalpy of formation obtained from expression(1) remains a key hypothesis of the thermodynamically stability and possible structurally synthesizability of our studied materials.

Table 1 Calculated structural equilibrium lattice constant a_0 , bulk modulus B , its pressure derivatives B' , ground state energies E_{\min} , and gap energy of the cubic SiLiX (X = Ca, Sr) in the three arrangements α (0.5, 0, 0.25), β (0.25, 0.5, 0), and γ (0, 0.25, 0.5)

Alloys	Type	State	a_0 (Å)	B (GPa)	B'	E_{\min} (Ry)	Gap (eV)	ΔH_f (eV)
SiLiCa	α	FM	6.88	25.5765	3.79	−1955.848439	0.685	−0.28
		PM	6.87	25.9688	3.44	−1955.841957	—	
	β	FM	6.80	30.2877	3.75	−1955.930038	1.209	
		PM	6.80	30.4951	3.60	−1955.926549	—	
	γ	FM	6.42	37.1518	3.60	−1955.925685	—	
		PM	6.42	36.3765	3.78	−1955.924198	—	
SiLiSr	α	FM	7.20	20.6965	3.55	−6954.734425	0.635	−0.72
		PM	7.20	20.1420	3.06	−6954.729804	—	
	β	FM	7.11	25.8347	3.87	−6954.828863	1.401	
		PM	7.13	24.7947	2.66	−6954.821473	—	
	γ	FM	6.72	31.2090	4.15	−6954.822323	—	
		PM	6.72	31.2462	4.10	−6954.822291	—	

$$\Delta H_f = E_{\text{tot}} - (E_{\text{Si}}^{\text{bulk}} + E_{\text{Li}}^{\text{bulk}} + E_{\text{X}}^{\text{bulk}}) \quad (1)$$

where E_{tot} and E_{bulk} denote respectively the total energy of the unit cell of the crystal and the energy of the related atom in solid state. The crystal structure of SiLiX alloy in the type β (FM) given in Fig. 2a, b was plotted by the CrystalMaker 2.7 software [41]. The structure is formed by three interpenetrating face-centered cubic sub-lattices, which are occupied by Si, Li, and Ca/Sr elements.

3.2 Electronic properties

In order to investigate the electronic properties of SiLiX (X = Ca and Sr) half-Heusler alloys, we computed the spin polarized band structures (BS) and their density of states (DOS) using the corresponding optimized lattice parameters, in the energy regions varying from −4 to 6 eV. The SiLiCa and SiLiSr alloys exhibit a quite similar band structure profile with an observable asymmetry between the spin-up and spin-down electronic channels, thus confirming the magnetic character of the compounds (Fig. 3a, b). For the both alloys, the electronic states proper to spin-down channel overlap and cross the Fermi level, which confirms the metallic behavior. Whereas, in the spin-up channel, the valence band maximum (VBM) and the conduction band minimum (CBM) are separated by energy band gap, which generates a semiconducting behavior. The VBM and the CBM arise at the Γ -X point giving an indirect bandgap of 1.209 eV in the case of SiLiCa alloy, while for the SiLiSr compound, the VBM and the CBM arise at the same X point providing so a direct bandgap of 1.401 eV. The half-metallicity can be stable that if the material possesses a large spin-flip gap (also known as half-metallic gap) [42]. The obtained half-metallic gap for the SiLiSr (0.42 eV) is double to that found for SiLiCa (0.21 eV). These values are considerably larger than those of other half-Heusler compounds containing transition metals; let us quote by

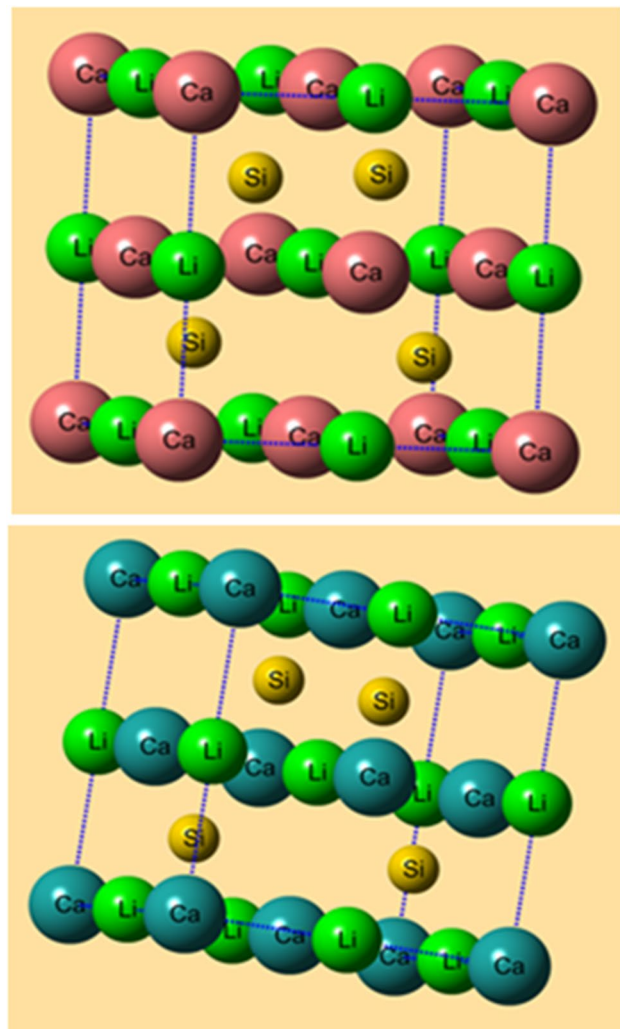
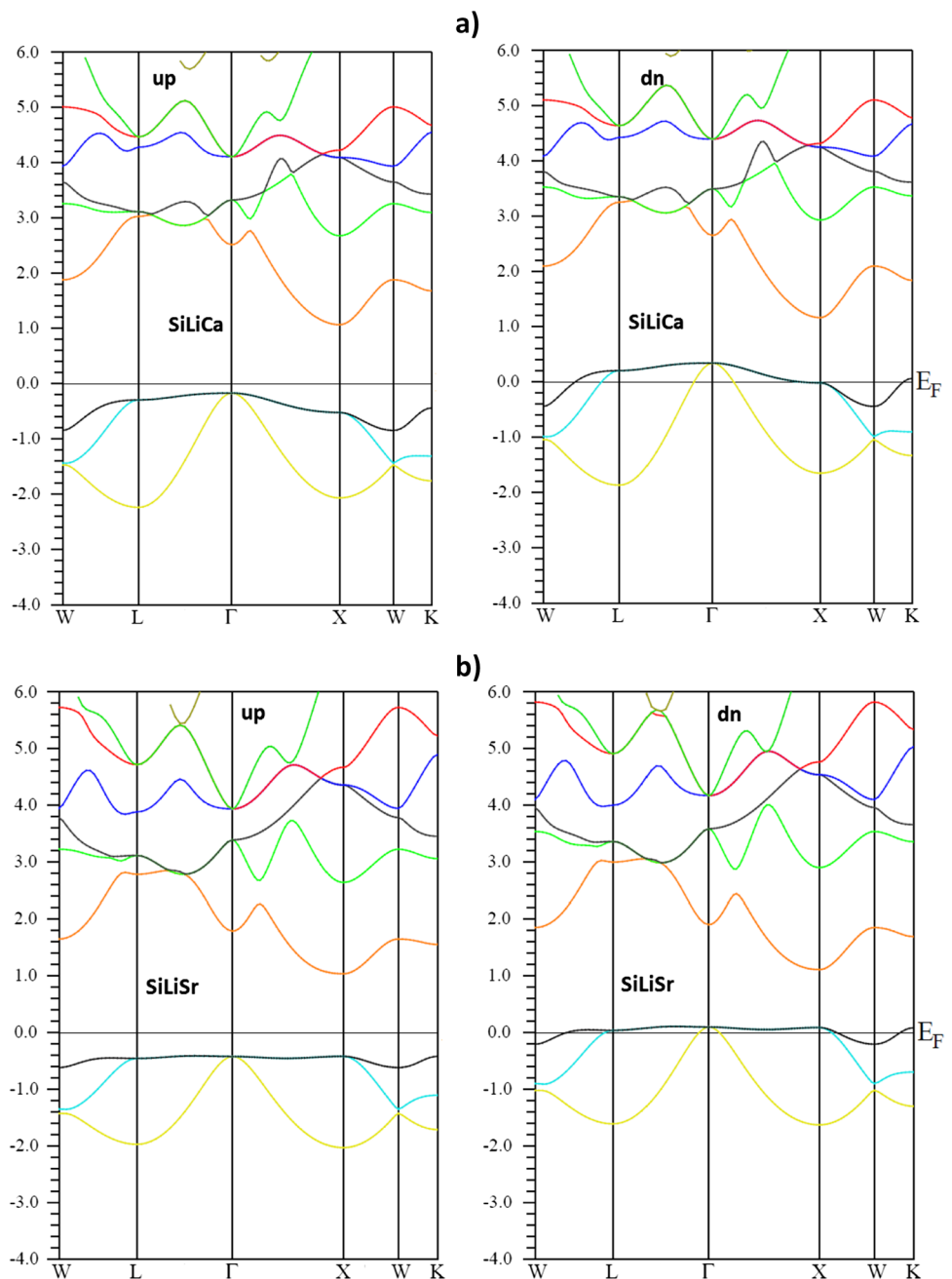


Fig. 2 The crystal structures of **a** SiLiCa and **b** SiLiSr compounds

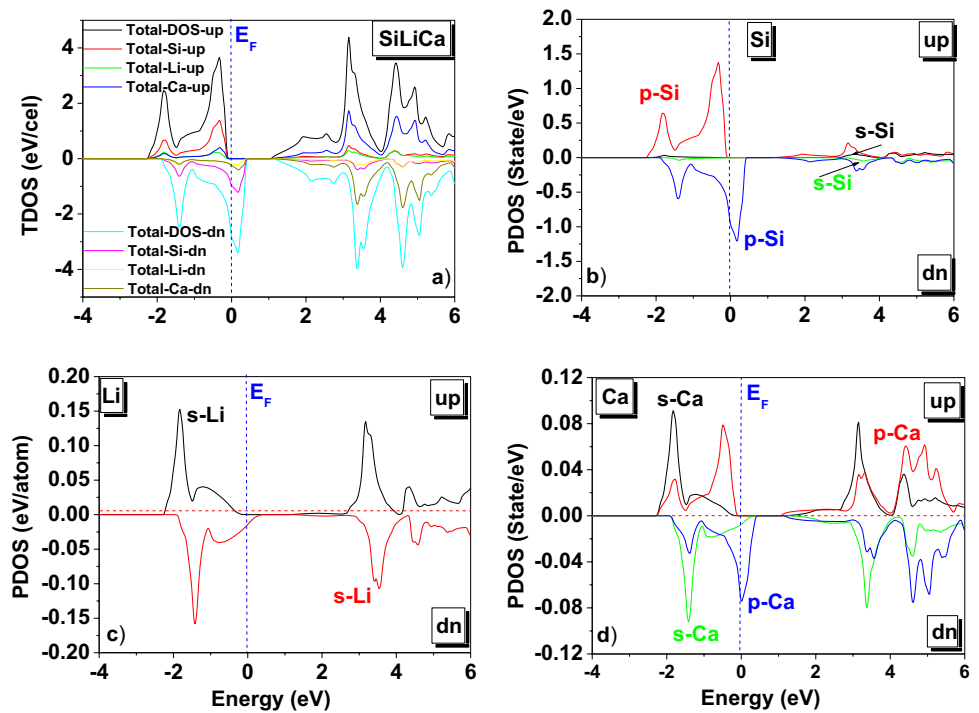
Fig. 3 Band structure of ferromagnetic SiLiX ($X = \text{Ca}$ and Sr) at the equilibrium lattice constant. Total and partial density of states (TDOS/PDOS) of SiLiCa. (Up: spin-up channel, dn: spin-down channel, E_F : Fermi level, and s, p are the electronic orbitals)



way of example 0.22 eV for CrVS [43], 0.17 eV for MnZrSi [44], and 0.05 eV for ErPdSb [45]. We can theoretically suggest good stability of half-metallic characteristics especially for the SiLiSr compound when it is incorporated in spintronic devices. Also, the flat band in the valence band displays the existence of heavy and light holes in SiLiSr alloy, which means that this compound is more effective in p-type than in n-type [46]. For examining the disposition of orbitals in the band structure and also to know which electrons are engaged in the shaping of the forbidden band, the total and partial density of the states

(TDOS/PDOSs) was plotted between -4 and 6 eV, where the dashed line shows the Fermi energy level (E_F). Figures 4a and 5a show the TDOS of the two alloys, an asymmetry between spin up (\uparrow) and spin down (\downarrow), is clearly visible which confirms the half-metallic character of SiLiX half-Heusler already predicted by band structure. For both compounds, the energy region around the Fermi level is mainly due to a major contribution of Si-p states (Fig. 4b and Fig. 5b) and a low contribution of Ca-p/Sr-p states (Fig. 4b and Fig. 5d), while the contribution of Li-s state is very minimal (Fig. 4c and Fig. 5c). The combined effect

Fig. 4 Total and partial density of states (TDOS/PDOS) of SiLiCa



of the crystal field and atoms constituting the alloy induces magnetism. From Table 2, we can see that the total magnetic moment for the two alloys is exactly $1.00 \mu_B$, which reveals the HM character of these alloys. The contribution of the interstitial site and partially filled p states of silicon

generates this total moment. In these Half-metallic ferromagnets alloys without transition metals, the Li and Ca (Sr) atoms play a capital role in the origin of magnetism although their contributions in the total magnetic moment value are negligible. This kind of alloy is very adapted

Fig. 5 Total and partial density of states (TDOS/PDOS) of SiLiSr. (Up: spin-up channel, dn: spin-down channel, E_F : Fermi level, and s, p are the electronic orbitals)

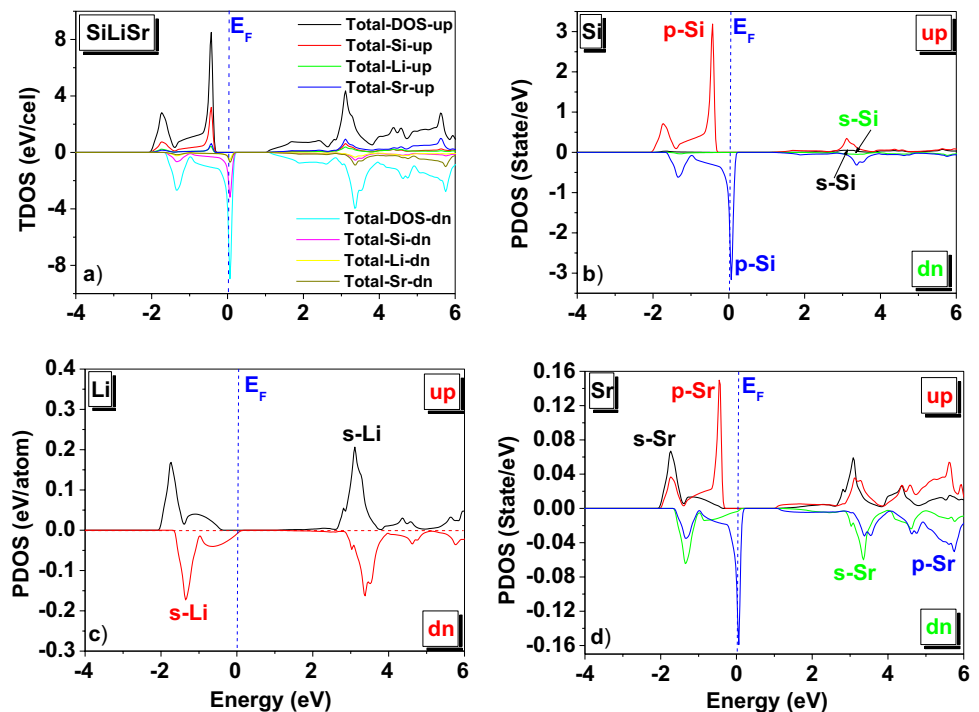


Table 2 Calculated individual, interstitial and total magnetic moments per formula units, half-metallic gaps (HM) and energy gaps E_g of the SiLiX (X = Ca and Sr) half-Heusler

	Method	μ_{Si} (μ_{B})	μ_{Li} (μ_{B})	$\mu_{\text{Ca/Sr}}$ (μ_{B})	μ_{inters} (μ_{B})	μ_{tot} (μ_{B})	HM gap (eV)	E_g (eV)	Band gap
SiLiCa	GGA-PBE	0.42469	0.04827	0.09393	0.43314	1.00	0.21	1.209	Γ -X
SiLiSr		0.42852	0.03632	0.06560	0.47044	1.00	0.42	1.401	X-X

in many applications, because a low magnetic moment implies less parasitic flow, which allows having a good efficiency of the magnetic circuits [47].

3.3 Optical properties

We present in this section the optical performances of the new d^0 half-Heusler alloys SiLiX (X = Ca, Sr). In order to describe the interaction of photons with SiLiX (X = Ca and Sr) alloys, the calculation of optical properties such as polarization, absorption, reflectivity, and refractive index is necessary. All the optical properties cited above derive from the complex dielectric function $\epsilon(\omega)$ (Eq. 2).

$$\epsilon(\omega) = \epsilon_1(\omega) + i\epsilon_2(\omega) \quad (2)$$

where $\epsilon_2(\omega)$ represents the real transition between the occupied and unoccupied states while $\epsilon_1(\omega)$ depicts the electronic polarizability under incident light [48]. The imaginary part of the dielectric function $\epsilon_2(\omega)$ is derived from the electronic band structure computations with the help of the following relation

$$\epsilon_2(\omega) = \left(\frac{4\pi^2 e^2}{m^2 \omega^2} \right) \sum_{i,j} \int \langle i | M | j \rangle^2 f_i (1 - f_j) \delta(E_j - E_i - \omega) d^3k \quad (3)$$

where e , m , ω and M represent the electron charge, electron mass, photon frequency, and dipole matrix, respectively. E_i is the electron energy of the initial state, E_j is the electron energy of the final state, and f_i is the Fermi occupation factor of the single-particle state i . The real part $\epsilon_1(\omega)$ of the dielectric function derives from $\epsilon_2(\omega)$ by using the Kramer–Kronig relations [49–51]:

$$\epsilon_1(\omega) = 1 + \frac{2}{\pi} P \int_0^{\infty} \frac{\omega' \epsilon_2(\omega')}{\omega'^2 - \omega^2} d\omega' \quad (4)$$

where P is the Cauchy principal value.

Other optical parameters like the absorption coefficient $\alpha(\omega)$, reflectivity $R(\omega)$, and refractive index $n(\omega)$ can be obtained from the calculated values of the real and imaginary parts of the dielectric function [52]:

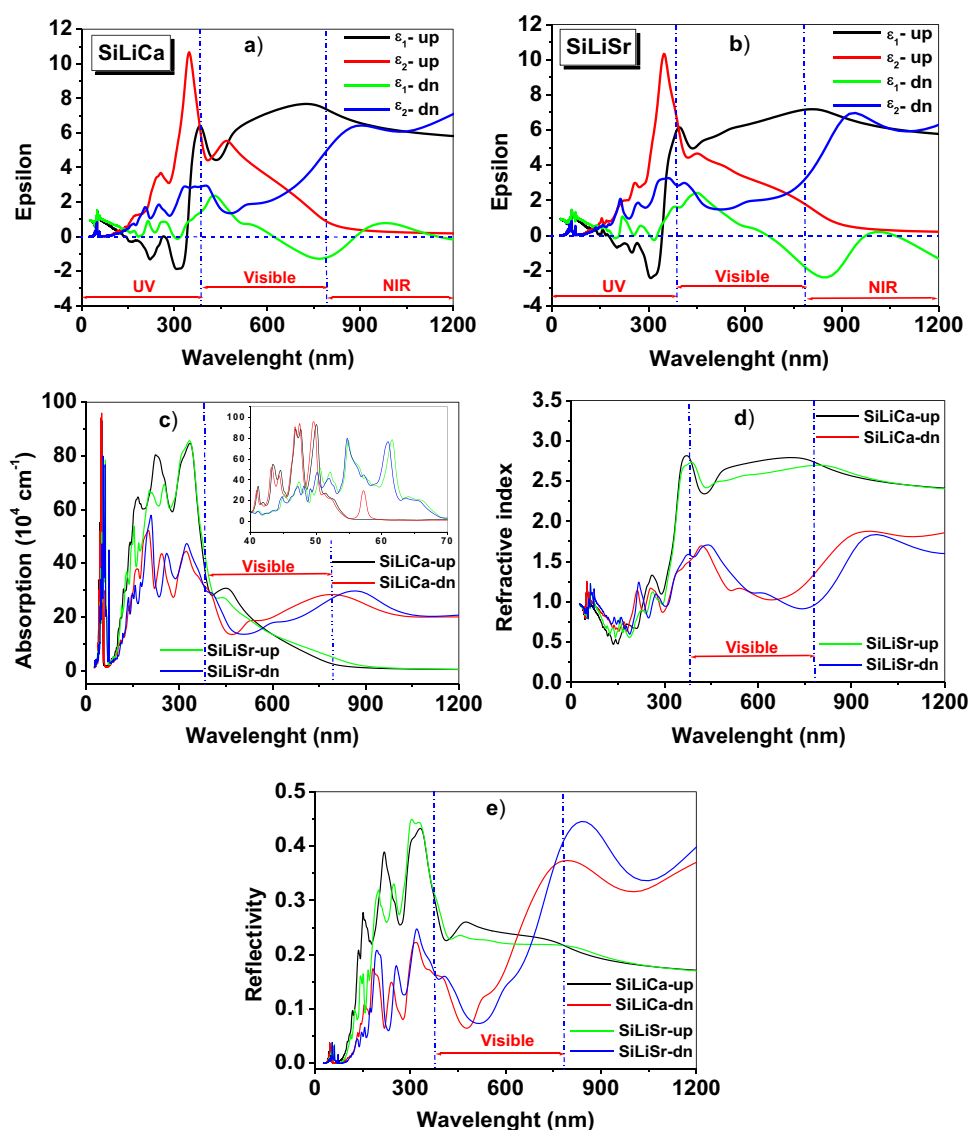
$$\alpha(\omega) = \frac{\sqrt{2}\omega}{c} \left(\sqrt{\epsilon_1^2(\omega) + \epsilon_2^2(\omega)} - \epsilon_1(\omega) \right)^{1/2} \quad (5)$$

$$R(\omega) = \left| \frac{\sqrt{\epsilon(\omega)} - 1}{\sqrt{\epsilon(\omega)} + 1} \right|^2 \quad (6)$$

$$n(\omega) = \left[\frac{\sqrt{\epsilon_1^2(\omega) + \epsilon_2^2(\omega)} + \epsilon_1(\omega)}{2} \right]^{1/2} \quad (7)$$

The majority of the optical properties such as absorption coefficient, reflectivity, and refractive index are derived from the dielectric function, which is obtained from the Kramer–Kronig dispersion relation [53–55]. As the lattice parameters are constant (cubic structure), the obtained optical responses are isotropic (same dielectric tensor). The variation versus energy of $\epsilon_1(\omega)$ which describes the slowing down of light in a material is shown in Fig. 6a, b. One can see that the SiLiX compounds respond strongly to the excitations of UV light; several peaks are visible in this domain; let us quote: $\lambda = 47, 60, 211, 204, 244,$ and 346 nm. $\epsilon_1(\omega)$ shows positive values meaning that the photons propagate through the material in these regions, and also shows negative values meaning that the compound completely reflects the incident radiation and exhibits a metallic character in these domains. The light absorption by the solid is explained by $\epsilon_2(\omega)$; this is associated to the absorption of the incident energy due to the different electronic transitions caused by the impact energies greater than the band gap. $\epsilon_2(\omega)$ attains in the UV domain its maximum value of 10.75 (10.28) for SiLiCa and SiLiSr respectively. We can see also that $\epsilon_2(\omega)$ shows several absorption peaks located at 45, 202, 246, 257, and 347 nm for SiLiCa alloy and 58, 154, 211, 255, 263, and 352 nm for SiLiSr compound. According to the total and partial density of states (TDOS/PDOS) (Figs. 4 and 5), these peaks can be related to the inter-band transitions between Si-3p, Li-2s, and Ca/Sr-4s/5s states. From the plot giving the evolution of absorption versus wavelength $\alpha(\omega)$, we can clearly see that the main absorption of the SiLiX compounds is located in the UV region; a maximum of 96.10^4 cm^{-1}

Fig. 6 Computed spin and wavelength dependent plots of **a, b** real and imaginary parts of the dielectric function, **c** absorption coefficient, **d** refractive index, and **e** reflectivity of SiLiX (X=Ca and Sr) compounds



is observed at 47.64 nm. We notice in the UV region that due to its direct bandgap, the SiLiSr compound responds more quickly by exhibiting peaks at energies of 20.32 eV (61 nm) and 23 eV (54 nm) giving an absorption coefficient of around 78.10^4 cm^{-1} . For the SiLiCa alloy, the transitions characterized by more intense absorption, which is close to 92.10^4 cm^{-1} , are observed at much more higher energies of 25.3 eV (49 nm) and 27 eV (46 nm). In addition, an absorption around 31.10^4 cm^{-1} is observed at 455 nm (visible) and 871 nm (NIR). The absorption coefficient for both compounds is almost constant for photon energies greater than the gap (879 nm for SiLiSr and 1025 nm for SiLiCa). The profile of the refractive index $n(\omega)$ follows the same pattern as that of the real part of the dielectric function because $n(\omega)$ and $\epsilon_1(\omega)$ both give the amount of light, which is slowed down in a light absorbing medium (Fig. 6d). In all two structures, $n(\omega)$ reaches a maximum in the ultraviolet (UV)

region and the maxima are obtained at 329 nm (3.77 eV) and 302 nm (4.11 eV) for X=Ca and Sr, respectively. $n(\omega)$ remains positive in the considered range of energy; this is due to the linearity of SiLiX to the frequency of light [56]. The reflectivity $R(\omega)$, which describes the ratio between the reflected energy to total incident energy, is plotted versus wavelength in Fig. 6e. We can plainly see that $R(\omega)$ appears across the electromagnetic spectrum of light (UV–VIS–NIR) and reaches its maximum in the negative range of $\epsilon_1(\omega)$. An utmost of 45% is observed at 301 nm (UV) and at 841 nm (NIR), values that are mostly due to the Plasmon resonance [57]. The minimum values of $R(\omega)$ are observed for wavelengths below than 100 nm (UV range), whereas above 100 nm (UV–visible domain), the value of $R(\omega)$ is greater than 6%. The decreasing reflectivity profile in the visible domain implies that a substantial amount of photon energy is transmitted through the material. The SLiX alloys can be

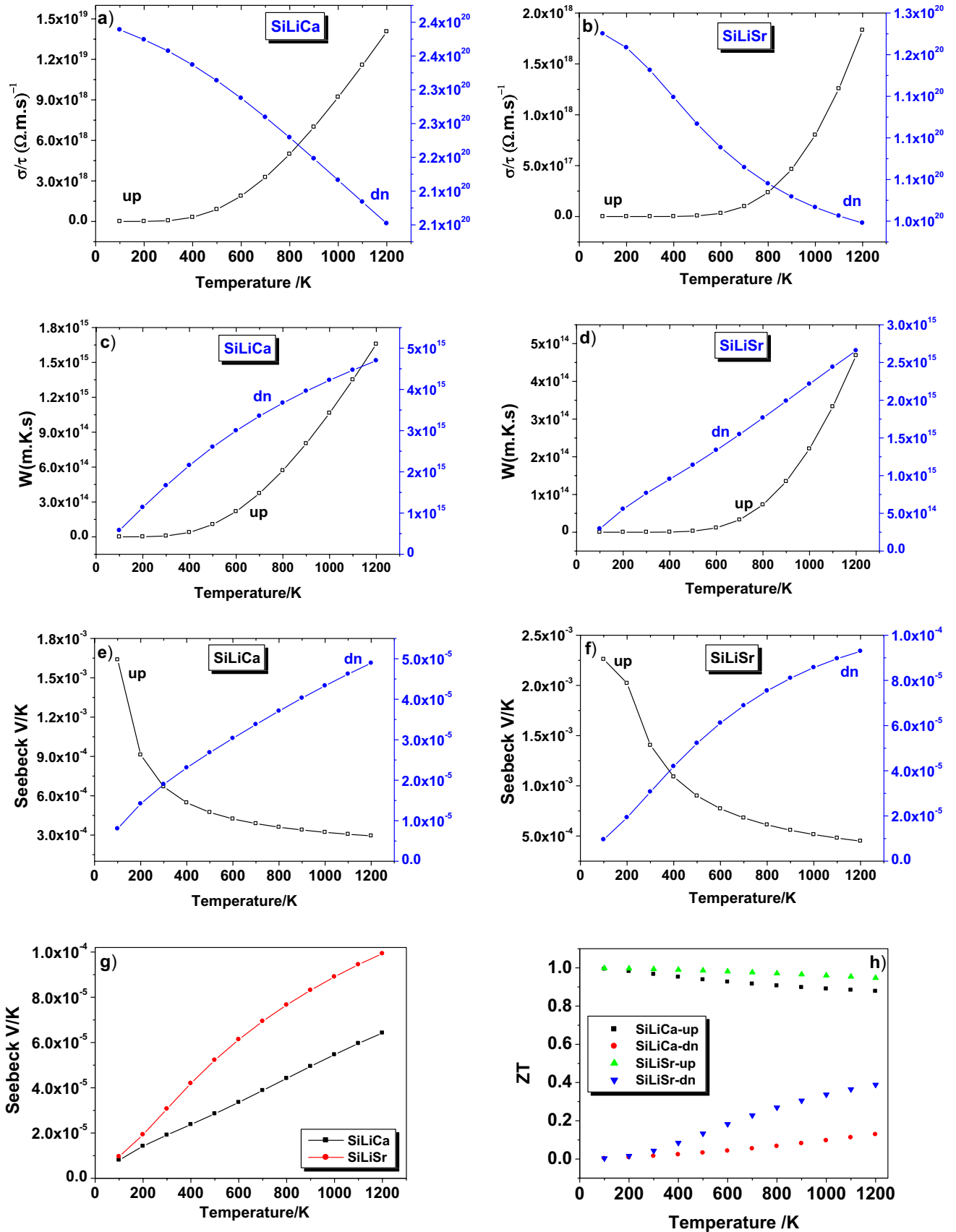


Fig. 7 Computed spin and temperature dependent plots of **a, b** electrical conductivity (σ/τ), **c, d** thermal conductivity (k/τ), **e–g** Seebeck coefficient (S), and **h** Merit factor (zT)

used as effective shields in large field of the electromagnetic spectrum of light, in particular in ultraviolet (UV) and near infrared (NIR) region.

3.4 Thermoelectric properties

The electronic transport responses of SiLiX ($X = \text{Ca, Sr}$) have been studied by employing the semi-classical Boltzmann theory equation [58, 59] within constant relaxation time approach [60] as implemented in Wien2K package [61].

$$\sigma_{\alpha\beta}(\mathbf{T}, \mu) = \frac{1}{\Omega} \int \sigma_{\alpha\beta}(\epsilon) [-\partial f_{\mu}(\mathbf{T}, \epsilon)] d\epsilon \quad (8)$$

$$\kappa_{\alpha\beta}(\mathbf{T}, \mu) = \frac{1}{e^2 T \Omega} \int \sigma_{\alpha\beta} \epsilon (\epsilon - \mu)^2 \frac{\partial f_{\mu}(\mathbf{T}, \epsilon)}{d\epsilon} \quad (9)$$

$$S = \frac{e}{T\sigma} \int \sigma_{\alpha\beta}(\epsilon) (\epsilon - \mu) \left[\frac{-\partial f_{\mu}(\mathbf{T}, \epsilon)}{\partial \epsilon} \right] \quad (10)$$

$$ZT = \frac{S^2 \sigma T}{\kappa} \quad (11)$$

where $\Omega, f, \mu, \sigma, \kappa, S$ and Z represent the unit-cell volume, Fermi–Dirac distribution function, chemical potential, electrical conductivity, thermal conductivity, Seebeck coefficient, and merit factor respectively. A clear idea about the thermoelectric efficiency of materials may be drawn by the calculation of the electrical conductivity (σ/τ), thermal conductivity (κ/τ), Seebeck coefficient (S), and merit factor (zT). The best thermoelectric materials (TE) must have great values of Seebeck coefficient and electrical conductivity associated to small thermal conductivity values [62]. The electrical conductivity, which means the flux of loose electrons in materials, remains a key parameter in the thermoelectricity. Figure 7a, b give, for the SiLiX ($X = \text{Ca, Sr}$) half-metallic alloys, the evolution of σ/τ versus temperature. For both compounds, the spin-up channel shows a significantly expansion of the σ/τ with temperature, so confirming the semiconducting behavior already predicted by the band structure, while for the spin-down configuration, σ/τ decreases with temperature, thereby indicating the metallic behavior. In the spin-up state, σ/τ increases from 5.67×10^{16} (2.03×10^{15}) $\Omega^{-1} \text{ m}^{-1} \text{ s}^{-1}$ at 100 K to 71.39×10^{19} (1.82×10^{18}) $\Omega^{-1} \text{ m}^{-1} \text{ s}^{-1}$ at 1200 K and in spin-down states, σ/τ decreases from 2.38×10^{20} (1.22×10^{20}) $\Omega^{-1} \text{ m}^{-1} \text{ s}^{-1}$ at 100 K to 2.11×10^{20} (9.97×10^{19}) $\Omega^{-1} \text{ m}^{-1} \text{ s}^{-1}$ at 1200 K,

for SiLiCa and SiLiSr respectively. Below 300 K for SiLiCa and 500 K for SiLiSr, the electrical conductivity values are not influenced by changing the levels of temperature. The evolution of thermal conductivity (κ/τ) against temperature for SiLiX ($X = \text{Ca, Sr}$) half-Heusler alloys is depicted in Fig. 7c, d. A quasi-linear profile between κ/τ and temperature is observed. In the spin-up case (semiconductor), κ/τ profile is the same to the electrical conductivity except that here the temperature change has a significant influence on the κ/τ values. It is seen that the κ/τ values increase radically with increase in temperature, attaining at 1200 K, the maximum values of 1.65×10^{15} (4.5×10^{14} W/mKs) for spin-up and 4.73×10^{15} (2.72×10^{15} W/mKs) for spin-down, respectively for SiLiCa and SiLiSr alloys. For spin-up channel, the κ/τ values are very weak until 400 K for SiLiCa and 600 K for SiLiSr, and beyond these temperatures, the κ/τ values increase significantly. The elevated temperatures improve the heat conduction through the electronic vibrations and cause an increase in thermal conductivity. The Seebeck coefficient (S) for SiLiX in both the spin configurations as a function of temperature is plotted in Fig. 7e, f. For the spin-up state, we observe an exponential decreasing trend of S ; this decrease in the magnitude of S with temperature mainly comes from the position of the Fermi level of the conduction band. An exponential increasing trend is remarked in both materials for the spin-down channel. Comparatively to the SiLiCa compound, the SiLiSr alloy is regarded as good candidate to the thermoelectric technology; it shows a flatness of the band near the Fermi level due to its effective mass which is large; this gives it great Seebeck coefficient (S) [63, 64]. We employed the two-current model [65, 66] to estimate the total Seebeck coefficient established from the materials (Eq. 12).

$$S = \frac{\sigma(\uparrow)S(\uparrow) + \sigma(\downarrow)S(\downarrow)}{\sigma(\uparrow) + \sigma(\downarrow)} \quad (12)$$

where $\sigma(\uparrow)$ and $\sigma(\downarrow)$ are electrical conductivities and $S(\uparrow)$ and $S(\downarrow)$ are Seebeck coefficients in spin-up and spin-down channels, respectively. We can see from Fig. 7g that for both compounds, the total S values increase linearly with increasing temperature. The positive sign of total S suggests that holes are the majority charge carriers in both the materials (p-type nature). This trend of behavior gives to these materials the compatibility for high-temperature thermoelectric applications. The calculated value of total S at 300 K is $19.52 \mu\text{V/K}$ for SiLiCa and $30.97 \mu\text{V/K}$ for SiLiSr. In order to evaluate the thermoelectric yield of SiLiX alloys upon a wide temperature range, the merit factor (zT) was computed by the relation $zT = S^2 \sigma T / \kappa$, where S, σ, T , and κ are Seebeck coefficient, electronic conductivity, absolute temperature, and thermal conductivity respectively. From Fig. 7h, we can observe that the zT curves show for the spin-up

Table 3 The calculated values of electrical conductivity, thermal conductivity, Seebeck coefficient, and merit factor for SiLiCa and SiLiSr in both spin configurations at room temperature

Alloys	Spin state	σ/τ ($\Omega^{-1} \text{ m}^{-1} \text{ s}^{-1}$)	κ/τ ($\text{WK}^{-1} \text{ m}^{-1} \text{ s}^{-1}$)	S (V K^{-1})	zT
SiLiCa	Up	8.13×10^{16}	6.62×10^{12}	6.70×10^{-4}	0.97
	Down	2.35×10^{20}	1.67×10^{15}	1.89×10^{-5}	0.04
SiLiSr	Up	7.03×10^{15}	3.51×10^{11}	1.40×10^{-3}	0.99
	Down	1.18×10^{20}	7.56×10^{14}	3.08×10^{-5}	0.01

channel, a slight linear decreasing trend as the temperature increase. At the room temperature, SiLiCa gives a value of 0.96 while SiLiSr achieves 0.99 and at high temperature (900 K), SiLiCa presents a value of 0.90 against 0.96 for SiLiSr. For both compounds, the merit factor remains higher than 0.9 in wide temperature range (100–900 K). The SiLiSr proves to be more efficient than SiLiCa at the temperature range considered due to its lower value of the thermal conductivity (Fig. 7d) as well as its nearly flat band located in the valence band of the energy band curve (Fig. 3b). The numerical values of some thermoelectric properties given at room temperature are presented in Table 3. We conclude that the zT remains the strong point of our alloys; it is close to unity in a very wide temperature range. At 300 K, it is definitely higher to those reported for other half-metallic ferromagnetic materials such as EuCrO₃ (~0.12) [67], RhFeGe (~0.94) [68], LaCoCrGa (~0.23), and LaCoCrAl (~0.43) [69]. Therefore, the SiLiX alloys meet the criteria, which suggest that in order to have peak performance from a thermoelectric power generator, a high zT value approaching ~1 is required.

4 Conclusion

Based on the full potential linearized augmented plane wave (FP-LAPW) method within the framework of generalized gradient approximation (GGA), the electronic, optical, and thermoelectric properties of the new d^0 half-Heusler alloys SiLiX (X = Ca, Sr) were studied in this article. The optimization provides that the FM phase is most stable than the PM phase. The electronic band structures and densities of states reveal ferromagnetic half-metallic behavior of SiLiCa and SiLiSr ternary half-Heusler compounds. Despite the absence of atoms with d or f layers, the SiLiX compounds present the same magnetic moment of 1 μ_B . The high peaks of the absorption coefficient $\alpha(\omega)$ detected in the UV zone and the high reflectivity, which is much greater than 43% in the UV and 38% in the NIR zone, allow our alloys to be used as UV photodetectors, UV filters, or as an effective shield in these areas. The change of various transport coefficients reflects the p-type character of the SiLiX alloys. The replacement of

calcium atom by a heavier element, strontium, shows large impact on the thermal conductivity, which has been reduced by 54% at room temperature. The merit factor values, which remain higher than 0.95 in large temperature range, affirm that the SiLiSr alloy in particular can be used for energy conversion and be used as alternative green energy sources.

Declarations

Conflict of interest The authors declare no competing interests.

References

1. R. De Groot, F. Mueller, P. Van Engen, K. Buschow, New class of materials: half-metallic ferromagnets. *Phys. Rev. Lett.* **50**(25), 2024 (1983)
2. Y. Gupta, M.M. Sinha, S.S. Verma, Theoretical study of thermodynamical and thermoelectric properties of novel half-Heusler alloys AlNiAs and AlNiSb. *Mater. Today. Commun.* **27**, 102195 (2021)
3. J. Nagura, T.M. Ashani, P.O. Adebambo, F. Ayedun, G.A. Adebayo, Thermoelectric and mechanical properties of XHfSn (X=Ni, Pd and Pt) semiconducting Half-Heusler alloys: a first-principles study. *Comput. Condens. Matter* **26**, e00539 (2021)
4. Y. Gupta, M.M. Sinha, S.S. Verma, Investigations of mechanical and thermoelectric properties of AlNiP novel half-Heusler alloy. *Mater. Chem. Phys.* **265**, 124518 (2021)
5. A. Besbes, R. Djelti, B. Bestani, O. Akel, First principles study of structural, electronic, thermodynamic, and thermoelectric properties of a new ternary half-Heusler alloy PdZrGe. *Chin. J. Phys.* **56**, 2926–2936 (2018)
6. F. Parvin, M.A. Hossain, I. Ahmed, K. Akter, A.K.M.A. Islam, First-principles calculations to investigate mechanical, optoelectronic and thermoelectric properties of half-Heusler p-type semiconductor BaAgP. *Res. Phys.* **23**, 104068 (2021)
7. H. Joshi, D.P. Rai, L. Hnamte, A. Laref, R.K. Thapa, A theoretical analysis of elastic and optical properties of half Heusler MCoSb (M[Ti, Zr and Hf]). *Heliyon* **5**, e01155 (2019)
8. A. Besbes, R. Djelti, B. Bestani, Optical and thermoelectric response of RhTiSb half-Heusler. *Int. J. Mod. Phys.* **33**(22), 1–12 (2019)
9. N. Nik-Akhtar, A. Vaez, Topological phase and optical properties of bulks and nanolayers of ScNiX (X = Ga and In) half-Heusler compounds. *Physica E* **103**, 164–170 (2018)
10. Yang Zhou, Jian-Min Zhang, Yu-Hong Huang, Xiu-Mei Wei, The structural, electronic, magnetic and mechanical properties of d^0 binary Heusler alloys XF₃ (X = Be, Mg, Ca, Sr, Ba), *Journal of Physics and Chemistry of Solids* **138** (2020) 109246.

11. S. Benatmane, S. Cherid, Ab initio study of the magnetism and half-metallic properties of d^0 quaternary Heusler alloys BaNYO ($Y = \text{K, Rb, and Cs}$). *JETP Lett.* **111**(12), 694–702 (2020)
12. Jiangtao Du, Shengjie Dong, Yi-Lin Lu, Hui Zhao, Liefeng Feng, L.Y. Wang, Half-metallic ferromagnetic features in d^0 quaternary-Heusler compounds KCaCF and KCaCCl : a first-principles description, *Journal of Magnetism and Magnetic Materials* 428 (2017) 250–254
13. M. Kazemi, P. Amiri, H. Salehi, Density functional study of d^0 half-metallic ferromagnetism in a bulk and (001) nano-surface of KP compound. *Phys. Lett. A* **381**, 2420–2425 (2017)
14. R. Ray, A.K. Himanshu, P. Sen, U. Kumar, M. Richter, T.P. Sinha, Effects of octahedral tilting on the electronic structure and optical properties of d^0 double perovskites A_2ScSbO_6 ($\text{A}=\text{Sr, Ca}$). *J. Alloy. Compd.* **705**, 497–506 (2017)
15. J.I. Beltrán, C. Monty, L.I. Balcells, C. Martínez-Boubeta, Possible d^0 ferromagnetism in MgO . *Solid. State. Commun.* **149**, 1654–1657 (2009)
16. T. Malsawmtluanga, B. Vanlalruata, R. Thapa, Investigation of half-metallicity of GeKMg and SnKMg by using mBJ potential method. *J. Phys. Conf. Ser.* 765, 012018 (2016) IOP Publishing.
17. A. Lakdja, H. Rozale, A. Chahed, O. Benhelal, Ferromagnetism in the half-Heusler XC_3Ba compounds from first-principles calculations ($X = \text{C, Si, and Ge}$). *J. Alloy. Compd.* **564**, 8–12 (2013)
18. H. Rozale, A. Amar, A. Lakdja, A. Moukadem, A. Chahed, Half-metallicity in the half-Heusler RbSrC , RbSrSi and RbSrGe compounds. *J. Magn. Magn. Mater.* **336**, 83–87 (2013)
19. G.Y. Jun Chen, K.L. Yao, Gao, M.H. Song, Half-metallic ferromagnetism in the half-Heusler compounds GeKCa and SnKCa from first-principles calculations. *J. Alloy. Compd.* **509**, 10172–10178 (2011)
20. L. Beldi, Y. Zaoui, K.O. Obodo, H. Bendaoud, B. Bouhafs, d^0 half-metallic ferromagnetism in GeNaZ ($Z = \text{Ca, Sr, and Ba}$) ternary half-Heusler alloys: an ab initio investigation. *J. Supercond. Novel Magn.* **33**, 3121–3132 (2020)
21. D.M. Hoat, J.F. Rivas-Silva, A. Méndez. Blas, Search for new d^0 half-metallic materials: theoretical investigation on $\text{KCaC}_{1-x}\text{Six}$ ($x = 0; 0.25; 0.5; 0.75$ and 1) compounds, *Chinese Journal of Physics* 56 (2018) 3078–3084.
22. R. Benabboun, D. Mesri, A. Tadjer, A. Lakdja, O. Benhelal, Half-metallicity ferromagnetism in half-Heusler XCaZ ($X = \text{Li, Na; Z} = \text{B, C}$) compounds: an ab initio calculation. *J Supercond Nov Magn* **28**, 2881–2890 (2015)
23. X.-P. Wei, Y.-D. Chu, X.-W. Sun, J.-B. Deng, Y.-Z. Xing, Stability, electronic, magnetic and pressure effect of half-Heusler alloys CNaCa and SiNaCa : a first-principles study. *Superlattices Microstruct.* **74**, 70–77 (2014)
24. R. Umamaheswari, D. Vijayalakshmi, G. Kalpana, First-principles calculation of structural, electronic and magnetic properties of half-Heusler LiCaC and NaCaC compounds. *Phys. B* **448**, 256–259 (2014)
25. N.A. Vahabzadeh, A. Boochani, S.M. Elahi, H. Akbari, Thermodynamic phase diagram, half-metallic and optical properties of the Zr_2TiSi [111] films based on DFT. *SILICON* **12**, 2165–2178 (2020)
26. M. Ilkhani, A. Boochani, M. Amiri, M. Asshabi, D.P. Rai, Mechanical stability and thermoelectric properties of the PdZrTiAl quaternary Heusler: A DFT study. *Solid. State. Commun.* **308**, 113838 (2020)
27. D.P. Rai, Sandeep, A. Shankar, A.P. Sakhya, T.P. Sinha, R. Khenata, M.P. Ghimire and R.K. Thapa, Electronic and magnetic properties of X_2YZ and XYZ Heusler compounds: a comparative study of density functional theory with different exchange-correlation potentials, *Mater. Res. Express* 3 (2016) 075022.
28. D.P. Rai, C.E. Ekuma, A. Boochani, S. Solaymani, R.K. Thapa, Electronic structure and X-ray spectroscopy of $\text{Cu}_2\text{MnAl}_{1-x}\text{Ga}_x$. *J. Appl. Phys.* **123**, 161509 (2018)
29. L. Siakeng, G.M. Mikhailov, D.P. Rai, Electronic, elastic and X-ray spectroscopic properties of direct and inverse full Heusler compounds Co_2FeAl and Fe_2CoAl , promising materials for spintronic applications: a DFT+U approach. *J. Mater. Chem. C* **6**, 10341–10349 (2018)
30. D.P. Rai et al., Pressure dependent half-metallic ferromagnetism in inverse Heusler alloy Fe_2CoAl : a DFT+U calculations. *RSC Adv.* **10**, 44633–44640 (2020)
31. Lalrinkima et al., Perpendicular magnetocrystalline anisotropy energy (MAE) of 111-surface slab of Fe_2CoAl . *Mater. Res. Express* **7**, 064003 (2020)
32. J.P. Perdew, K. Burke, M. Ernzerhof, Generalized gradient approximation made simple. *Phys. Rev. Lett.* **77**, 3865–3868 (1996)
33. S. Adachi, Properties of semiconductor alloys: group-IV, III-V and II-VI semiconductors (John Wiley & Sons, 2009).
34. J. Sun, H.T. Wang, N.B. Ming, Optical properties of heterodiamond B_2CN using first-principles calculations. *Appl. Phys. Lett.* **84**, 4544 (2004)
35. J.M. Hu, S.P. Huang, Z. Xie, H. Hu, W.D. Cheng, First-principles study of the elastic and optical properties of the pseudocubic Si_3As_4 , Ge_3As_4 and Sn_3As_4 . *J. Phys. Condens. Matter* **19**, 496215 (2007)
36. G.K.H. Madsen, D.J. Singh, BoltzTraP: A code for calculating band-structure dependent quantities. *Comput. Phys. Commun.* **175**, 67 (2006)
37. A.R. Mishra, S. Pal, First-principles calculations to investigate electronic structure and magnetic, mechanical and thermodynamic properties of d^0 half-Heusler LiXN ($X = \text{Na, K, Rb}$) alloys. *Solid-state. Sci.* **118**, 106633 (2021)
38. S. Benatmane, B. Bouhafs, Investigation of new d^0 half-metallic full-Heusler alloys N_2BaX ($X = \text{Rb, Cs, Ca and Sr}$) using first-principle calculations. *Comput. Condens. Matter.* **16**, e00371 (2019)
39. D.M. Hoat et al., Search for new d^0 half-metallic materials: theoretical investigation on $\text{KCaC}_{1-x}\text{Six}$ ($x = 0; 0.25; 0.5; 0.75$ and 1) compounds, *Chinese Journal of Physics* 56 (2018) 3078–3084.
40. S. Parsamehr, A. Boochani, M. Amiri, S. Solaymani, E. Sartipi, S. Naderi, A. Aminian, Thermodynamic phase diagram and thermoelectric properties of LiMgZ ($Z = \text{P, As, Bi}$): ab initio method study. *Phil. Mag.* **101**(3), 369–386 (2021)
41. CrystalMaker software, crystalmaker, on-line URL <http://www.crystallmaker.com>.
42. D.M. Hoat, Duc-Quang Hoang, Mosayeb Naseri, R. Ponce-Pérez, Nguyen T.T. Binh, J.F. Rivas-Silva, Gregorio H. Coccoletzi, New equiatomic quaternary Heusler compounds without transition metals KCaBX ($X = \text{S and Se}$): robust half-metallicity and optical properties, *Journal of Molecular Graphics and Modelling* 100 (2020) 107642
43. M. Javed, M.A. Sattar, M. Benkraouda, N. Amrane, Structural and mechanical stability, lattice dynamics and electronic structure of the novel CrVZ ($Z = \text{S, Se, Te}$) half-Heusler alloys. *Mater. Today. Commun.* **25**, 101519 (2020)
44. E.G. Ozdemir, Z. Merdan, First principle predictions on half-metallic results of MnZrX ($X = \text{In, Tl, C, Si, Ge, Sn, Pb, N, P, As, Sb, O, S, Se, Te}$) half-Heusler compounds. *J. Magn. Magn. Mater.* **491**, 165567 (2019)
45. J. Kumar Satyam, S. Mohan Saini, Electronic structure and optical properties of Rare-Earth based ErPdSb half Heusler Compound: A GGA + U study. *Mater. Today. Proc.* **44**, 3040–3044 (2021)
46. A. Page, P.F.P. Poudeu, C. Uher, A first-principles approach to half-Heusler thermoelectrics: accelerated prediction and understanding of material properties. *J. Materiomics* **2**, 104–113 (2016)

47. A. Abada, N. Marbough, Study of new d^0 half-metallic half-Heusler alloy MgCaB: first-principles calculations. *J. Supercond. Novel Magn.* **33**, 889–899 (2020)
48. B. Amin, I. Ahmad, M. Maqbool, S. Goumri-Said³, and R. Ahmad, Ab initio study of the bandgap engineering of $Al_{1-x}Ga_xN$ for optoelectronic applications, *J. Appl. Phys.* **109**, (2011) 023109
49. G. Marius, *The Physics of Semiconductors: Kramers-Kronig Relations* (Springer, Berlin Heidelberg, 2010), pp. 775–776
50. M. Gajdoš, K. Hummer, G. Kresse, J. Furthmüller, F. Bechstedt, Linear optical properties in the projector-augmented wave methodology. *Phys. Rev. B.* **73**, 045112 (2006)
51. C. Ambrosch-Draxl, J.O. Sofo, Linear optical properties of solids within the full potential linearized augmented planewave method. *Comput. Phys. Commun.* **175**, 1–14 (2006)
52. M. Irfan, M.A. Kamran, S. Azam, M.W. Iqbal, T. Alharbi, A. Majid, S.B. Omran, R. Khenata, A. Bouhemadou, X. Wang, Electronic structure and optical properties of TaNO: an ab initio study. *J. Mol. Graph. Model.* **92**, 296–302 (2019)
53. K. Yamamoto, H. Ishida, Kramers-Kronig analysis applied to reflection absorption spectroscopy. *Vib Spectrosc.* **15**, 27–36 (1997)
54. H.C. Kandpal, G.H. Fecher, C. Felser, Calculated electronic and magnetic properties of the half-metallic, transition metal based Heusler compounds. *J. Phys. D Appl. Phys.* **40**, 1507 (2007)
55. M.L. Cohen, J.R. Chelikowsky, *Electronic Structure and Optical Properties of Semiconductors*, 2nd edn. (Springer-Verlag, Berlin, 1989)
56. N. Yaqoob et al., Structural, electronic, magnetic, optical and thermoelectric response of half-metallic $AMnTe_2$ ($A = Li, Na, K$): an ab-initio calculations. *Physica. B. Conden. Matter.* **574**, 311656 (2019)
57. A. Benzina, First-principles calculation of structural, optoelectronic properties of the cubic $Al_xGa_yIn_{1-x-y}N$ quaternary alloys matching on AlN substrate, within modified Becke-Johnson (mBJ) exchange potential. *Optik* **127**, 11577–11587 (2016)
58. D. Vasileska, H.R. Khan, S.S. Ahmed, G. Kannan, C. Ringhofer, *Quantum and Coulomb Effects in Nano Devices* (Springer, Nano-Electronic Devices, 2011), pp. 97–181
59. A. Reshak, Thermoelectric properties of the spin-polarized half-metallic ferromagnetic CsTe and RbSe compounds. *RSC Adv.* **6**, 98197–98207 (2016)
60. Y. Kimura, A. Zama, Thermoelectric properties of p-type half-Heusler compound HfPtSn and improvement for high-performance by Ir and Co additions. *Appl. Phys. Lett.* **89**, 172110 (2006)
61. P. Blaha, K. Schwarz, G.K.H. Madsen, D. Kvasnicka, J. Luitz, *WIEN2k, An Augmented Plane Wave plus Local Orbitals Program for Calculating Crystal Properties* (Vienna University of Technology, Austria, 2001), p. 269
62. A. Abada, N. Marbough, Study of new d^0 half-metallic half-Heusler alloy MgCaB: first-principles calculations. *J. Supercond. Nov. Magn.* **33**, 889–899 (2020)
63. J. Yang, P. Qiu, R. Liu, L. Xi, S. Zheng, W. Zhang, L. Chen, D.J. Singh, Trends in electrical transport of p-type skutterudites RFe_4Sb_{12} ($R = Na, K, Ca, Sr, Ba, La, Ce, Pr, Yb$) from first-principles calculations and Boltzmann transport theory. *Phys. Rev. B* **84**, 235205 (2011)
64. Sapan Mohan Saini, Structural, electronic and thermoelectric performance of narrow gap LuNiSb half Heusler compound: Potential thermoelectric material, *Physica B* **610** (2021) 412823.
65. T.M. Bhat, S. Singh, D.C. Gupta, Electronic and transport properties of $LaNi_4Sb_{12}$ skutterudite: modified Becke-Johnson approach. *J. Electron. Mater.* **47**, 4544–4549 (2018)
66. H.J. Xiang, D.J. Singh, suppression of thermopower of Na_xCoO_2 by an external magnetic field: Boltzmann transport combined with spin-polarized density functional theory. *Phys. Rev. B* **76**, 195111 (2007)
67. R. Ullah, M. Azmat Ali, G. Murtaza, A. Mahmood, S.M. Ramay, An investigation of structural, elastic, mechanical, electronic, magnetic and thermoelectric properties of ferromagnetic half metallic $EuCrO_3$. *Mater. Sci. Semicond. Process.* **122**, 105487 (2021)
68. M.A. Bennani, Z. Aziz, S. Terkhi, E.H. Elandaloussi, B. Bouadjemi, D. Chenine, M. Benidris, O. Youb, S. Bentata, Structural, electronic, magnetic, elastic, thermodynamic, and thermoelectric properties of the half-Heusler $RhFeX$ (with $X = Ge, Sn$) compounds. *J. Supercond. Novel Magn.* **34**, 211–225 (2021)
69. S. Singh, D.C. Gupta, Lanthanum based quaternary Heusler alloys $LaCoCrX$ ($X=Al, Ga$): hunt for half-metallicity and high thermoelectric efficiency. *Res. Phys.* **13**, 102300 (2019)